# Roles of Point Defects in Thermal Transport in Perovskite Barium Stannate

Liang Chen,[†] Yingying Zhang,[‡] Xiaojia Wang,[‡,§] Bharat Jalan,[∥] Shuangtao Chen,[*,†] and Yu Hou[†]

[†]School of Energy and Power Engineering, Xi'an Jiaotong University, Xi'an 710049, China
[‡]Department of Mechanical Engineering, [§]Department of Electrical and Computer Engineering, and [∥]Department of Chemical Engineering and Materials Science, University of Minnesota, Minneapolis, Minnesota 55455, United States

Ⓢ Supporting Information

ABSTRACT: Perovskite barium stannate ($BaSnO_3$) is a promising candidate that can be used as transparent conducting oxide in optoelectronic devices and as the channel material in high-mobility oxide electronics. In this work, we calculate the lattice thermal conductivity and investigate the impact of point defects on thermal transport in $BaSnO_3$ based on the phonon Boltzmann transport equations with interatomic force constants from first-principles calculations. In pristine $BaSnO_3$, we find the contribution of acoustic phonons to thermal transport accounts for 54% at 300 K and the rest is attributed to the lower-frequency (27.5−50 THz) optical modes with relatively high group velocity. We show

oxygen vacancies and impurities can cause noticeable reduction in thermal conductivity of $BaSnO_3$, but the corresponding mechanisms differ in terms of scattering rates on different phonon modes. The thermal conductivity reduction due to oxygen vacancies at 300 K is mainly caused by the increased scattering of the acoustic phonons and the low-frequency optical phonons. Lanthanum and potassium impurities mainly increase the scattering of acoustic phonons, but antimony impurity lowers the thermal conductivity by increasing the scattering rate of dominant phonons, including both the acoustic modes and the low-frequency optical modes. The results and findings facilitate us to better understand the thermal transport mechanisms of perovskite oxides with an emphasis on the impact of oxygen vacancies and impurities on the thermal properties of $BaSnO_3$.
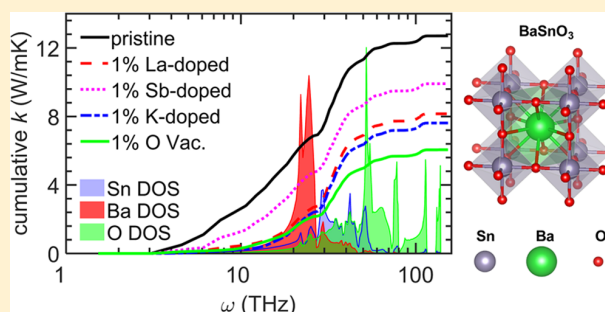
I. INTRODUCTION

Transparent conducting oxides (TCOs) with high electrical conductivity and high optical transmission[1] have great potential for many applications, e.g., solar cells,[2] light-emitting diodes,[3] displays,[4] and gas sensors.[5] Among a wide variety of oxides, the perovskite barium stannate ($BaSnO_3$) has recently gained increasing attention as next-generation TCO materials due to its excellent electrical properties and superior thermal stability[6] at high temperatures. It has been demonstrated that $BaSnO_3$ has a wide bandgap ($\sim$3.0 eV)[7,8] and thermal stability at the temperature up to 1000 °C.[6] In previous studies[9−14] of $BaSnO_3$, the electrical properties have been extensively investigated, but only a few studies[15−18] have focused on the thermal properties, which are critical for heat dissipation in electronic devices with high power or under extreme conditions. In this work, we report a comprehensive investigation on the phonon property and thermal conductivity of perovskite $BaSnO_3$ based on the first-principles calculations and the phonon Boltzmann transport equations (BTEs).

To obtain a high electron mobility in $BaSnO_3$, one has to modify its band structures via control of the cation doping[9,12−14,19,20] and oxygen vacancies.[21] It has been shown that an electron mobility as high as 320 cm^2 V^{-1} s^{-1} can be achieved at room temperature (300 K) in lanthanum (La)-

doped bulk single crystal.[6] Previous studies have demonstrated the point defects induced by the impurity and vacancy can have different impacts on the thermal transport in various materials.[22−24] Here, we show that the impurities and oxygen vacancies can significantly lower the thermal conductivity of $BaSnO_3$ and the spectral dependence of defect scattering can lead to different reductions of thermal conductivity. We find the impurities and oxygen vacancies cause the increase of phonon scattering rate via different channels. The findings have implications more widely for perovskite oxides with the ABO_3 structure that are used as transparent conducting materials.

We compare the first-principles predictions of heat capacity and thermal conductivity with the experimental data available in the literature,[7,15] which show reasonable agreement. We further quantify different impacts of scattering due to point defects by comparing the thermal properties of $BaSnO_3$ with other perovskites.[25−28] This work will thus constitute a comprehensive study on the thermal conductivity of $BaSnO_3$ as well as the impact of impurities and oxygen vacancies, which is important

for developing advanced TCO materials with desirable thermal properties.

II. MODELS AND COMPUTATIONAL METHODS

II.I. First-Principles Calculations. In this study, the open-source code Quantum Espresso[29] is employed to perform first-principles density function theory (DFT) calculations including lattice optimization and calculations for the second-order and third-order interatomic force constants. The interactions of core electrons are described using the norm-conserving pseudo-potentials, and the exchange and correlation energy are calculated by the general gradient approximation with a Troullier−Martins-type[30] Perdew−Burke−Ernzerhof[31] functional. The kinetic energy cutoff for wave functions is 80 Ry in all calculations. In the lattice optimization, DFT calculations are performed on a primitive perovskite unit cell of $BaSnO_3$ with 5 atoms and $9 \times 9 \times 9$ k-point grids. The optimized lattice constant is 4.199 Å, which is 2% larger than the experimental value of 4.117 Å.[32]

The second-order interatomic force constants are computed on a primitive unit cell using density functional perturbation theory[33] on a $4 \times 4 \times 4$ q-point grid. The third-order interatomic force constants are determined using the finite difference method. A displacement of 0.01 Å is systematically applied on the selected atoms of the supercell with a $3 \times 3 \times 3$ supercell with 135 atoms. We use a Python tool[34] to create the lattice structures with displacement and to calculate the third-order interatomic force constants based on the DFT calculations for forces. Convergence tests are performed for the calculations of both the second-order and third-order force constants. The phonon dispersion and lattice thermal conductivity are also computed on a $5 \times 5 \times 5$ q-point grid and a $4 \times 4 \times 4$ supercell with 320 atoms, respectively. As detailed in the Supporting Information, a good convergence can be achieved with a $4 \times 4 \times 4$ q-point grid and a $3 \times 3 \times 3$ supercell for the second-order and third-order force constants, respectively.

II.II. Thermal Conductivity Calculations. On the basis of the second- and third-order force constants from first-principle calculations, the thermal conductivity of the bulk $BaSnO_3$ of pristine lattice can be obtained by solving the linearized phonon Boltzmann transport equations using the single-mode relaxation time approximation or an iterative approach.[35] Under the relaxation time approximation, the intrinsic three-phonon scatting rate ($\Gamma_{j\mathbf{q}}^{\text{anh}}$) can be determined using Fermi's Golden rule.[22]

The oxygen vacancies and impurities are treated as point defects, and the distribution of the defects is random and uniform. In this study, the scattering rate contribution from the point defects is estimated using Green's function approach, which considers the perturbations of both the mass and the interatomic force constants.[23,36] It should be noted that the local change in the interatomic force constants around the impurity atom may cause significant scattering for certain structures. For example, boron impurities in zinc-blende SiC can break the structural symmetry around the boron atoms, resulting in the resonant phonon scattering and a significant reduction in thermal conductivity.[37] The scattering rate for phonon mode $|j\mathbf{q}\rangle$ is given by

$$\Gamma_{j\mathbf{q}}^{\text{def}} = \pi\chi_{\text{def}}\frac{\Omega}{V_{\text{def}}}\frac{1}{\omega_{j\mathbf{q}}}\sum_{j'\mathbf{q}'}|\langle j'\mathbf{q}'|\mathbf{T}|j\mathbf{q}\rangle|^2\delta(\omega_{j'\mathbf{q}'}{}^2 - \omega_{j\mathbf{q}}{}^2)$$

where χ_{def} is the number fraction of defects, V_{def} is the volume of a defect, and Ω is the volume of the unit cell. The **T** matrix is computed from retarded Green's function ($\mathbf{g}^+$) of the pristine lattice and the perturbation matrix (**V**), which is given by

$$\mathbf{T} = (\mathbf{I} - \mathbf{V}\mathbf{g}^+)^{-1}\mathbf{V}$$

Both the contributions from the changes to the atomic mass and force constant are included in the perturbation matrix, e.g., $\mathbf{V} = \mathbf{V}^M + \mathbf{V}^K$. The perturbation matrix of mass difference is diagonal with nonzero elements corresponding to the onsite terms for the defect atom i.

$$\mathbf{V}_{ii}{}^M = -\frac{M_i' - M_i}{M_i}\omega^2$$

where M_i' and M_i are the masses of the defective and original atoms at the ith site, respectively. The perturbation matrix of force constants $\mathbf{V}^K$ is computed from the difference between the interatomic force constants for the defective lattice ($\mathbf{K}'$) and perfect lattice ($\mathbf{K}$) as

$$\mathbf{V}_{i,j}{}^K = \frac{\mathbf{K}'_{i,j} - \mathbf{K}_{i,j}}{\sqrt{M_i M_j}}$$

For the oxygen vacancy, no defective atom is introduced in the lattice and the perturbation matrix $\mathbf{V}^K$ is the only term in the calculation of vacancy scattering rate.

The final scattering rate $\Gamma_{j\mathbf{q}}$ is calculated according to Matthiessen's rule.[38]

$$\Gamma_{\mathbf{jq}} = \Gamma_{\mathbf{jq}}^{\text{anh}} + \Gamma_{\mathbf{jq}}^{\text{def}}$$

We note the coupling between phonon−phonon and phonon-impurity scattering may lead to a different thermal conductivity. As demonstrated by the previous molecular dynamics simulations,[39,40] the spectral Matthiessen's rule neglects the coupling term of scattering rate and overestimates the thermal conductivity of doped silicon by about 20−40% at a concentration of 1%. In this study, we employ first-principles calculations to predict the thermal conductivity and the direct simulation of a large supercell with 1% concentration will not be affordable. The coupling effects between $\Gamma_{j\mathbf{q}}^{\text{anh}}$ and $\Gamma_{j\mathbf{q}}^{\text{def}}$ are not considered or evaluated.

The force constants of atoms around the impurity or vacancy defect are calculated using a $3 \times 3 \times 3$ supercell with one defect atom. The retarded Green's function of the pristine lattice is computed on an $18 \times 18 \times 18$ q-point grid with the analytical tetrahedron method proposed by Lambin and Vigneron.[41] The tests for the q-point grid selection and the validation of numerical calculation are performed, as detailed in the Supporting Information.

With the **T** matrix, the cross sections $\sigma_{j\mathbf{q}}$ of the phonon-defect scattering are computed and relates the scattering rate as

$$\Gamma_{\mathbf{jq}}^{\text{def}} = \frac{\chi_{\text{def}}}{V_{\text{def}}}\sigma_{\mathbf{jq}}|v_{\mathbf{jq}}|$$

where $v_{j\mathbf{q}}$ is the phonon group velocity. The cross sections for phonon-defect scattering are exported to the open-source package (ShengBTE),[35] and the solution of phonon Boltzmann transport equations is performed using an iterative approach. Both the phonon−phonon scattering rate and phonon-defect scattering rate are computed on a $20 \times 20 \times 20$ q-point grid. Convergence tests for the BTE calculations are performed, and the variation of thermal conductivity of pristine BSO at 300 K is

less than 1% if the q-point grid is further refined from $20 \times 20 \times 20$ to $24 \times 24 \times 24$.

III. RESULTS AND DISCUSSION

III.I. Phonon Properties. The perovskite $BaSnO_3$ has a lattice structure with space group $Fm\overline{3}m$, and the cubic unit cell is shown in Figure 1a. The Ba, Sn, and O ions occupy the body
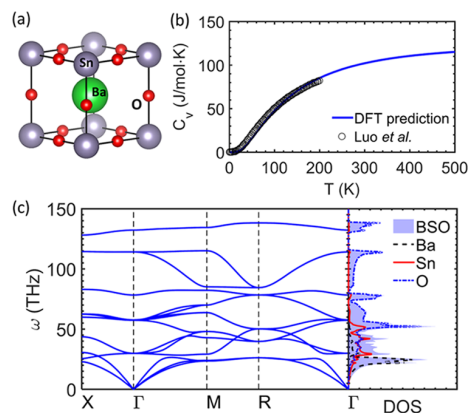
**Figure 1.** (a) Cubic perovskite structure of $BaSnO_3$; (b) constant volume heat capacity as a function of temperature and comparison with experimental values by Luo et al.;[7] (c) phonon dispersion curves (left) and partial density of states (DOS) (right) of $BaSnO_3$.

center, corners, and edge centers of the cubic cell, respectively. The experimental lattice constant of 4.117 Å[16,32] is used in the first-principles calculations for phonon properties and thermal conductivity. We also optimize the cubic unit cell by minimizing the total energy with respect to the cell parameters, giving a computed optimized lattice constant of 4.199 Å, which is larger than the experimental value by 2%. On the basis of the second-order interatomic force constants from first-principles calculations, the phonon properties are determined by the lattice dynamics calculations. Figure 1b compares our model's calculated values of constant volume heat capacity with the experimental values by Luo et al.,[7] indicating a good agreement up to 200 K.

The phonon dispersion relations of $BaSnO_3$ as shown in Figure 1c are calculated along the symmetry lines in the first Brillouin zone. By applying acoustic sum rules[42] to the second-order interatomic force constants, the three acoustic branches all converge to 0 THz at γ point and no imaginary mode is observed, indicating the stability of the lattice structure. A small phonon frequency gap can be observed at M point between 82.2 and 85.1 THz, which is consistent with a previous study.[43] Figure 1c also shows the phonon density of states (DOS) of $BaSnO_3$ and the partial DOS associated with the Ba, Sn, and O atoms. It can be observed that the acoustic phonon modes populate the DOS up to 27.5 THz, whereas the optical modes mainly constitute the region between 27.5 and 140 THz. The partial DOS of an atom is calculated by projecting the vibration polarization vector of this atom onto the Cartesian axes. The partial DOS in Figure 1c indicates the population of lower-frequency modes below 27 THz is mainly contributed by the partial DOS of the heavier Ba atom. The partial DOS of Sn atoms mainly contributes to the total DOS in the intermediate frequency region from 27 to 56 THz. The partial DOS of O atoms predominates the phonon DOS beyond 56 THz.

III.II. Thermal Conductivity of Pristine $BaSnO_3$ and Phonon Contributions. We first compute the lattice thermal conductivity of the pristine $BaSnO_3$ by solving the linearized phonon Boltzmann transport equations with a relaxation time approximation and then with an iterative approach. It has been demonstrated that the electronic contribution to the thermal conductivity of the conducting $BaSnO_{3-\delta}$ is only around 4% based on the measurements of electrical conductivity and the Wiedemann−Franz law. Therefore, phonons dominate the thermal transport in both the pristine $BaSnO_3$ and the doped $BaSnO_3$.

Figure 2a compares the lattice thermal conductivity of the iterative solution to that of the relaxation time approximation
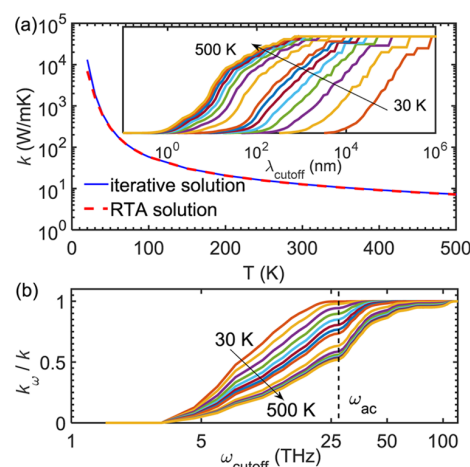
Figure 2. (a) Thermal conductivity of pristine $BaSnO_3$ as a function of temperature from an iterative solution and from a relaxation time approximation solution of phonon Boltzmann transport equation; (b) normalized cumulative thermal conductivity of pristine $BaSnO_3$ as a function of frequency cutoff (ω_{cutoff}) for different temperatures. The inset in (a) shows the normalized cumulative thermal conductivity as a function of phonon mean free path (MFP) cutoff (λ_{cutoff}) for different temperatures. The vertical dashed line in (b) denotes the frequency dominated by acoustic phonons (ω_{ac}).

solution for the pristine $BaSnO_3$. The difference is negligible except at very low temperatures below 20 K where the Umklapp scattering is considerably weaker.[44] This is because the relaxation time approximation treats the normal and Umklapp scattering as independent processes, resulting in underestimation of the thermal conductivity.[45] The calculations show the thermal conductivity at 300 K is 12.7 W m^{-1} K^{-1}, which is comparable to the values obtained from the 3ω measurement (13.2 W m^{-1} K^{-1})[15] and the time-domain thermoreflectance measurement (13.3 W m^{-1} K^{-1}).[18]

By integrating the phonon mode contribution to the thermal conductivity up to a chosen cutoff of the phonon mean free path (MFP), we obtain the cumulative thermal conductivity as a function of phonon MFP. The inset in Figure 2a shows the normalized cumulative thermal conductivity as a function of phonon MFP cutoff (λ_{cutoff}) for different temperatures. Normalization is performed with respect to the converged thermal conductivity at the corresponding temperature. It can be clearly observed that the MFP of the dominant phonon(s) decreases as the temperature increases due to the pronounced Umklapp scattering. The major contribution to thermal conductivity comes from phonons with MFP between 10^4
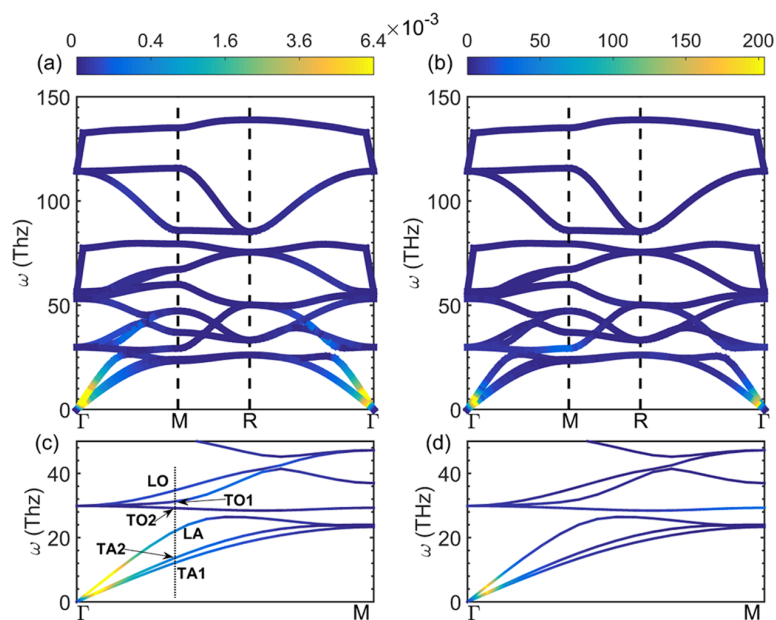
Figure 3. Phonon dispersion curves colored by (a) mode contribution to thermal conductivity of pristine BaSnO$_3$ and (b) phonon relaxation time; (c, d) zoom in the frequency region below 50 THz of (a) and (b), respectively. The color bar of (a) denotes ratio of mode contribution to the converged thermal conductivity, whereas the color bar of (b) denotes phonon relaxation time (in picosecond) at 300 K.
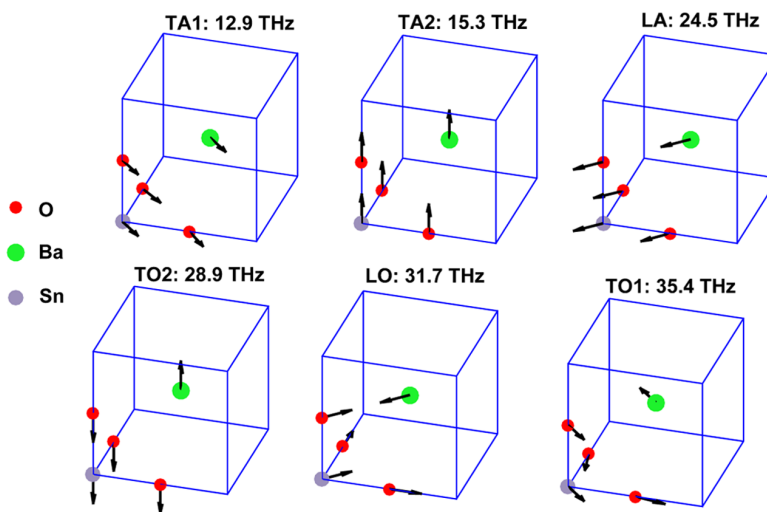
Figure 4. Eigenvectors of Ba, Sn, and O atoms in a cubic unit cell show the six phonon modes in Figure 3c,d, which are transverse acoustic mode 1 (TA1), transverse acoustic mode 2 (TA2), longitudinal acoustic mode (LA), transverse optical mode 2 (TO2), longitudinal optical mode (LO), and transverse optical mode 1 (TO1) from low frequency to high frequency.

and 10^6 nm at 30 K, whereas it shifted to phonons with MFP between 1 and 1200 nm at 300 K.

Similarly, we compute the cumulative thermal conductivity as a function of phonon frequency cutoff (ω_{cutoff}), as shown in Figure 2b. As the temperature increases, phonons with higher frequency are excited and their contribution to the thermal transport increases. The vertical dashed line in Figure 2b denotes the frequency of dominant acoustic phonons (ω_{ac}). We find the contribution of acoustic phonons to thermal transport accounts for 54% at 300 K, and the rest we attribute to the low-frequency (27.5−50 THz) optical modes. As the temperature decreases to 30 K, the thermal conductivity of pristine BaSnO$_3$ is primarily due to acoustic phonons. It is well established that the low-frequency phonons, which have long wavelengths, are

insensitive to point defects. Therefore, understanding the frequency-dependent phonon contribution can help explain the impact of impurities and vacancies on the thermal conductivity, which will be further discussed in the following sections.

To further illustrate the role of different phonon modes in the thermal transport of BaSnO$_3$, we show the mode contribution and phonon relaxation time on the dispersion curves, as shown in Figure 3a,b, respectively. The acoustic phonons, including the two transverse branches and one longitudinal branch, have large contribution to the thermal conductivity, associated with their large phonon relaxation times, which is consistent with the observation of accumulative thermal conductivity in Figure 2b. Compared with the transverse acoustic (TA) modes, the longitudinal acoustic

(LA) modes have a relatively larger contribution owing to their higher phonon group velocity.

It should also be noted that the optical phonons contribute 46% to the thermal transport in $BaSnO_3$ at 300 K. Those optical phonons mainly belong to the low-frequency (27.5−50 THz) range. It can be found from Figure 3 that the optical modes originating from 30 THz at the γ point have considerable contribution and relatively large phonon relaxation time compared with the rest of optical phonons. To identify the phonon mode of greatest contribution to the thermal conductivity, we show the eigenvectors of Ba, Sn, and O atoms in a cubic unit cell in Figure 4 for the phonon modes below 50 THz in Figure 3c, which are transverse acoustic mode 1 (TA1), transverse acoustic mode 2 (TA2), longitudinal acoustic mode (LA), transverse optical mode 2 (TO2), longitudinal optical (LO) mode, and transverse optical mode 1 (TO1) from low frequency to high frequency. As shown in Figure 3c,d, the LO and TO1 modes have relatively large contribution owing to their high group velocities. Although TO2 modes have larger relaxation time than that of TO1 and LO (see Figure 3d), they have negligible contribution to the thermal transport (see Figure 3c) due to the near-zero phonon group velocities.

III.III. Impact of Oxygen Vacancies. Because of the oxygen deficiency during the crystal growth of $BaSnO_3$ and the following procedures of electron doping, oxygen vacancies[20,21] frequently occur with sufficient concentration to affect the thermal conductivity.[46] We compute the thermal conductivity of $BaSnO_3$ with a fraction of oxygen vacancies up to 1% and find that the oxygen vacancies can considerably lower the thermal conductivity even at room temperature. Figure 5
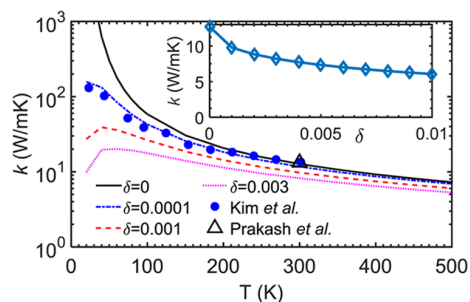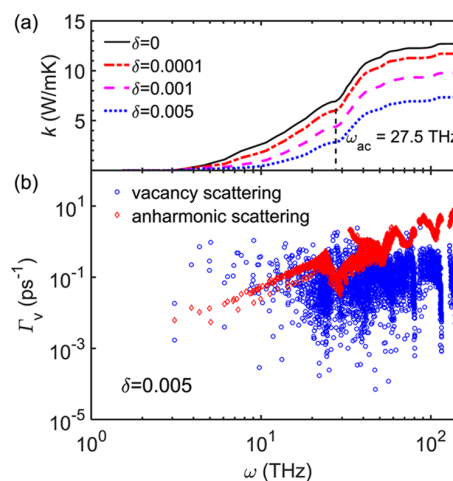

Figure 5. Thermal conductivity as a function of temperature for $BaSnO_3$ with different oxygen vacancy fractions. The blue solid dots denote the measurement results by Kim et al.[15] for $BaSnO_{3-\delta}$ with charge density around 10^{18} cm^{-3}, and the red hollow triangle denotes the measurement value by Prakash et al.[18] The inset shows the thermal conductivity at 300 K as a function of oxygen vacancy fraction.

compares the computed thermal conductivity of $BaSnO_3$ of different vacancy concentrations with the experimental results by Kim et al.[15] for $BaSnO_{3-\delta}$ with charge density around 3×10^{18} cm^{-3}. This low charge density is introduced by the slight oxygen vacancies, which are created during the flux growth procedure, and the corresponding vacancy fraction is around 1.0×10^{-4} if one oxygen vacancy introduces two free charges. As shown in Figure 5, good agreement can be reached between our computed values at a vacancy fraction of 1×10^{-4} and those experimental values[15] at temperatures up to 210 K. At 300 K, the thermal conductivity of $BaSnO_{3-\delta}$ by Kim et al. (13.2 W m^{-1} K^{-1})[15] is very close to that of the stoichiometric $BaSnO_3$ by Prakash et al. (13.3 W m^{-1} K^{-1}).[18] When the

temperature is above 210 K, our predictions are slightly lower than the experimental values. Our prediction of 12.7 W m^{-1} K^{-1} is within 5% lower than experimental values,[15,18] and this underestimation can be well explained by neglecting the electronic contribution (4%) to thermal transport in $BaSnO_3$.

As the temperature decreases, the impact of oxygen vacancies becomes more significant due to the reduced Umklapp scattering at low temperatures and the thermal conductivity tends to decrease for BSO with a higher vacancy fraction. The inset in Figure 5 shows the thermal conductivity at 300 K as a function of oxygen vacancy concentration. The vacancy fractions of 0.1 and 1% can lead to the reduction of thermal conductivity at 300 K by 23.2 and 52.3%, respectively. The oxygen vacancy level does not change the general temperature dependence of thermal conductivity.

To understand the role of oxygen vacancies in thermal transport in $BaSnO_3$, we present frequency-dependent cumulative thermal conductivity at 300 K and the scattering rates by oxygen vacancies at different concentration levels in Figure 6. The vertical dashed line in Figure 6a denotes the
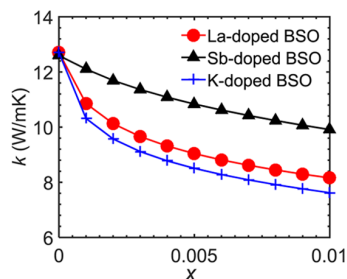

Figure 6. (a) Cumulative thermal conductivity at 300 K as a function of frequency cutoff for $BaSnO_3$ with different oxygen vacancy concentrations and (b) scattering rates by oxygen vacancy as a function of frequency at different concentrations. The vertical dashed line in (a) denotes the frequency dominated by acoustic phonons (ω_{ac} = 27.5 THz).

frequency of dominant acoustic phonons (ω_{ac} = 27.5 THz). At 300 K and a low vacancy fraction (0.01%), the major reduction (∼95%) in thermal conductivity occurs due to the scattering of acoustic phonon modes, whereas the contribution from phonons at frequencies above ω_{ac} is only weakly affected by the oxygen vacancies. At a relatively high vacancy fraction (∼0.5%), the decrease of acoustic phonon contribution accounts about 76% of the total reduction in thermal conduction. This observation can be further confirmed by the vacancy scattering rates shown in Figure 6b. In the frequency below ω_{ac}, the vacancy scattering rates are higher than the phonon anharmonic scattering, which leads to the major reduction of thermal conductivity, as shown in Figure 6a. As the vacancy fraction increases from 0.01 to 0.5%, further reduction of thermal conductivity is caused by the vacancy scattering of phonons in the frequency range from 27.5 to 40 THz, where

the vacancy scattering rates can be higher than the phonon anharmonic scattering rate.

III.IV. Impact of Impurity. The perovskite $BaSnO_3$ is usually doped with La, Sb, and K atoms to alter its electrical properties. An n-type semiconductor is obtained by substituting Ba^{2+} ions with La^{3+} ions in the La-doped $BaSnO_3$,[9] or by substituting Sn^{4+} ions with the Sb^{5+} ions in the Sb-doped $BaSnO_3$,[19] whereas a p-type semiconductor is obtained by substituting Ba^{2+} ions with the K^+ ions in the K-doped $BaSnO_3$.[20] We compute the thermal conductivity of $BaSnO_3$ with impurities of La, Sb, and K atoms from 0 to 1%, as shown in Figure 7. It can be observed that all of the three types of

Figure 8. (a) Cumulative thermal conductivity at 300 K for $BaSnO_3$ with impurities of lanthanum (La), antimony (Sb), and potassium (K) as a function of phonon frequency; (b) scattering rates by impurity as a function of frequency at 300 K. The impurity fraction is 1% for all of the three cases. The partial phonon density of states of Sn and Ba atoms are also illustrated in (a) by the shaded areas.

Figure 7. Thermal conductivity of $BaSnO_3$ doped by lanthanum (La), antimony (Sb), and potassium (K) as a function of impurity fraction.

impurities can lead to noticeable reduction in the thermal conductivity. At the same impurity fraction, e.g., 1% as in Table 1, the K-impurity can cause the largest reduction (40%) in the
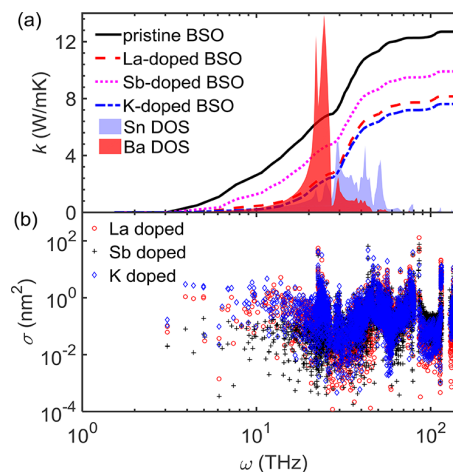
Table 1. Thermal Conductivity at 300 K for $BaSnO_3$ with Impurities of Lanthanum (La), Antimony (Sb), and Potassium (K) and Impurity Fraction of 1%[a]

dopant	k_{300K} (W m^{-1} K^{-1})	Δk (W m^{-1} K^{-1})	Δk_{ac} (W m^{-1} K^{-1})
Sb (1%)	9.9	2.8 (22.0%)	2.1 (76.1%)
La (1%)	8.2	4.5 (35.4%)	4.2 (94.0%)
K (1%)	7.6	5.1 (40.2%)	4.5 (87.6%)

[a]Δk is the reduction in thermal conductivity as compared with the thermal conductivity of pristine $BaSnO_3$ (12.7 W m^{-1} K^{-1}). Δk_{ac} denotes the reduction of thermal conductivity caused by the defect scattering of acoustic phonon modes. The values in the parentheses are the percentage changes.

thermal conductivity, whereas the Sb-impurity causes the least decrease (22%). It should be noted that the atomic weights of La (138.9) and Sb (121.8) atoms are close to those of Ba (137.3) and Sn (118.71) atoms, respectively. Therefore, the perturbation of mass difference contributes little to the impurity scattering by La and Sb and the major reduction should be attributed to the changes of interatomic force constants. The perturbation of mass difference (39.1 vs 137.3) by K-impurity is much higher than that of La and Sb impurities, which can lead to the largest reduction in the thermal conductivity of $BaSnO_3$.

It is worth noting that all of the three types of impurities can change the local chemical bonding properties due to the different electronic structures with that of original atom. The changes in the interatomic force constants can lead to a significant perturbation and increase the defect scattering. To explore the scattering mechanism by different impurities, we show the cumulative thermal conductivity and the cross section of defect scattering in Figure 8. From Figure 8a, we can find that the La-impurity and K-impurity have similar reduction of

accumulative thermal conductivity at a frequency below ω_{ac} (27.5 THz) and this frequency regime should be dominated by the perturbation in force constants. The reduction in thermal conductivity by La-impurity is only slightly lower than that by K-impurity. At a higher frequency, the scattering rate due to the mass difference becomes important, which leads to more reduction in the thermal conductivity of K-doped $BaSnO_3$. Figure 8b clearly illustrates that the scattering rates by La-impurity and K-impurity are similar in the frequency range below ω_{ac} and the scattering rates by K-impurity become higher as the frequency increases beyond ω_{ac}.

By measuring the difference in the accumulative thermal conductivity at ω_{ac} (27.5 THz), we show in Table 1 the reduction caused by the dopant-induced scattering of acoustic modes accounts for 76, 94, and 87.6% for Sb-impurity, La-impurity, and K-impurity, respectively. The rest of reduction is attributed to the defect scattering with the low-frequency optical modes (TO1 and LO). It is interesting that the reduction by Sb-impurity is much smaller than that by La-impurity and the defect scattering by Sb-impurity is relatively lower in the acoustic region. The different spectral scatterings with different impurity atoms can be explained by their spectral contribution to the DOS or the phonon partial DOS, as illustrated by the shaded area in Figure 8a. The phonon state population associated with Ba atom is dominant in the acoustic regime and thereby the increased scattering by the La- or K-impurities will be mainly observed in this frequency regime. Different from La- or K-impurity, the Sb-impurity substitutes the Sn atom, which has low-phonon population in the frequency region below 27.5 THz, but relatively high population in the frequency region between 27.5 and 60 THz. Therefore, the scattering rates by Sb-impurity are lower than those by La-impurity and K-impurity at low frequency but becomes higher in the frequency range between 27.5 and 60 THz. The low partial DOS of Sn atoms in the low-frequency regime avoids significant scattering of acoustic phonons and finally leads to relatively higher thermal conductivity than the La-impurity.

III.V. Discussion and Comparison with Other Perovskite Oxides. On the basis of the results shown in Figures 5 and 7, we show that point defects can considerably reduce the thermal conductivity. Among the approaches to increase the number of charge carriers in $BaSnO_3$,[9,19,20] the n-type Sb-impurity has relatively smaller effect on the thermal conductivity but the n-type La-impurity, O-vacancy, and the p-type K-impurity can considerably lower the thermal conductivity. In applications such as solar cells,[2] light-emitting diodes,[3] high-field transistors,[47] and power electronics,[14] a high thermal conductivity is desired for the purpose of efficient heat dissipation and from this point of view, the Sb-doping would be preferred.

The main advantage of $BaSnO_3$ compared to other perovskite oxides is its potential to achieve a high room-temperature electron mobility[6] with appropriate doping. Compared with the most-studied perovskite oxides,[1] such as $SrTiO_3$ and $KTaO_3$, for the thermal properties, $BaSnO_3$ has a room-temperature thermal conductivity (13 W m^{-1} K^{-1})[15] slightly higher than that of $SrTiO_3$ (11 W m^{-1} K^{-1})[48,49] but lower than that of $KTaO_3$ (17 W m^{-1} K^{-1}).[25] The dependence of these thermal conductivity values on temperature is, however, quite different. The thermal conductivity of pristine $BaSnO_3$ increases as temperature decreases to 20 K, whereas the thermal conductivities of $SrTiO_3$ and $KTaO_3$ reach a maximum value at temperatures between 50 and 100 K.[27,49] For the cation-doped $BaSnO_3$ and vacancy-doped $BaSnO_3$, the temperature dependence of thermal conductivity remains similar to that of the pristine $BaSnO_3$ in the studied range from 20 to 500 K, suggesting the minor role of defect scattering in the thermal transport in $BaSnO_3$ compared with the major role of inherent phonon–phonon scattering.[15]

Compared with $BaSnO_3$, the thermal conductivity of $SrTiO_3$ is not sensitive to the La-impurity but it is strongly affected by the oxygen vacancies.[49] It was shown that both the $Sr_{0.98}La_{0.02}TiO_3$ and $SrTiO_3$ have a thermal conductivity around 11 W m^{-1} K^{-1} at 300 K. In contrast, the thermal conductivities of oxygen-deficient $Sr_{0.98}La_{0.02}TiO_{3-\delta}$ grown at 650 and 450 °C were measured[49] to be ~3.88 and ~2.55 W m^{-1} K^{-1}, respectively, which were significantly lower than those of the unreduced $Sr_{0.98}La_{0.02}TiO_3$ and $SrTiO_3$ (11 W m^{-1} K^{-1}). For the $Sr_{0.98}La_{0.02}TiO_{3-\delta}$ grown at 450 °C,[49] a glasslike thermal transport behavior was observed,[50] meaning a positive temperature dependence of the thermal conductivity. This indicates a more important role of optical phonons in $SrTiO_3$.

IV. CONCLUSIONS

In summary, we have studied the role of phonon modes in the thermal transport in $BaSnO_3$ based on first-principles calculations and on the phonon Boltzmann transport equations and we have computationally investigated the impact of oxygen vacancies and impurities on the thermal conductivity of $BaSnO_3$. Our calculations of thermal conductivity of perovskite $BaSnO_3$ agree well with the previous experimental results. We find the contributions of acoustic phonons and the lower-frequency (27.5–50 THz) optical phonons dominate the thermal transport in pristine $BaSnO_3$ at 300 K. The oxygen vacancy and impurity can reduce the thermal conductivity considerably due to different phonon scattering mechanisms. For the thermal transport in $BaSnO_3$ at 300 K, the oxygen vacancy and antimony impurities increase the scattering of both the acoustic phonons and the low-frequency optical phonons, whereas the lanthanum and potassium impurities mainly increase the scattering of the acoustic phonons. The results and findings in this work can provide further insight into the phonon contribution to thermal transport in $BaSnO_3$ and can provide better understanding of the phonon scattering due to point defects in perovskite oxides.

■ ASSOCIATED CONTENT

ⓢ Supporting Information

The Supporting Information is available free of charge on the ACS Publications website at DOI: 10.1021/acs.jpcc.8b00653.

Convergence tests for the calculations of second-order force constants, third-order force constants, and Green's function (PDF)

■ AUTHOR INFORMATION

Corresponding Author

*E-mail: stchen.xjtu@mail.xjtu.edu.cn.

ORCID ⓘ

Liang Chen: 0000-0002-3767-3546

Bharat Jalan: 0000-0002-7940-0490

Notes

The authors declare no competing financial interest.

■ REFERENCES

(1) Lee, W.-J.; Kim, H. J.; Kang, J.; Jang, D. H.; Kim, T. H.; Lee, J. H.; Kim, K. H. Transparent Perovskite Barium Stannate with High Electron Mobility and Thermal Stability. *Annu. Rev. Mater. Res.* **2017**, *47*, 391−423.

(2) Lee, S.; Lee, C. W.; Kim, D. W.; Shin, S.; Jung, H. S.; Cho, S.; Kim, H.; Hong, K. S. BaSnO3 Perovskite Nanoparticles for High Efficiency Dye-Sensitized Solar Cells BaSnO3 Perovskite Nanoparticles for High Efficiency Dye-Sensitized Solar Cells. *ChemSusChem* **2013**, *6*, 449−545.

(3) Ohta, H.; Kawamura, K. I.; Orita, M.; Hirano, M.; Sarukura, N.; Hosono, H. Current Injection Emission from a Transparent P-N Junction Composed of P-SrCu∼2O∼2/n-ZnO. *Appl. Phys. Lett.* **2000**, *77*, 475−477.

(4) Nomura, K.; et al. Thin-Film Transistor Fabricated in Single-Crystalline Transparent Oxide Semiconductor. *Science* **2003**, *300*, 1269−1272.

(5) Alagdal, I. A.; West, A. R. Oxygen Stoichiometry, Conductivity and Gas Sensing Properties of BaSnO3. *J. Mater. Chem. C* **2016**, *4*, 4770−4777.

(6) Kim, H. J.; Kim, U.; Kim, H. M.; Kim, T. H.; Mun, H. S.; Jeon, B. G.; Hong, K. T.; Lee, W. J.; Ju, C.; Kimy, K. H.; Char, K. High Mobility in a Stable Transparent Perovskite Oxide. *Appl. Phys. Express* **2012**, *5*, No. 061102.

(7) Luo, X.; Oh, Y. S.; Sirenko, A.; Gao, P.; Tyson, T. A.; Char, K.; Cheong, S. W. High Carrier Mobility in Transparent Ba$_{1-x}$La$_x$SnO$_3$ Crystals with a Wide Band Gap. *Appl. Phys. Lett.* **2012**, *100*, No. 172112.

(8) Chambers, S. A.; Kaspar, T. C.; Prakash, A.; Haugstad, G.; Jalan, B. Band Alignment at Epitaxial BaSnO3/SrTiO3(001) and BaSnO3/

LaAlO$_3$(001) Heterojunctions. *Appl. Phys. Lett.* **2016**, *108*, No. 152104.

(9) Kim, H. J.; Kim, U.; Kim, T. H.; Kim, J.; Kim, H. M.; Jeon, B.; Lee, W.; Mun, H. S.; Hong, K. T.; Yu, J.; Char, K.; Kim, K. H. Physical Properties of Transparent Perovskite Oxides (Ba,La)SnO$_3$ with High Electrical Mobility at Room Temperature. *Phys. Rev. B* **2012**, *86*, No. 165205.

(10) Stanislavchuk, T. N.; Sirenko, A. A.; Litvinchuk, A. P.; Luo, X.; Cheong, S. Electronic Band Structure and Optical Phonons of BaSnO$_3$ Ba$_{0.97}$La$_{0.03}$SnO$_3$ Single Crystals: Theory and Experiment. *J. Appl. Phys.* **2012**, *112*, No. 044108.

(11) Soleimanpour, S.; Kanjouri, F. First Principle Study of Electronic and Optical Properties of the Cubic Perovskite BaSnO$_3$. *Phys. B* **2014**, *432*, 16–20.

(12) Prakash, A.; Xu, P.; Faghaninia, A.; Shukla, S.; Rd, A. J.; Lo, C. S.; Jalan, B. Wide Bandgap BaSnO$_3$ Films with Room Temperature Conductivity Exceeding 10^4 S cm^{-1}. *Nat. Commun.* **2017**, *8*, No. 15167.

(13) Paik, H.; Chen, Z.; Lochocki, E.; Seidner, A. H.; Verma, A.; Tanen, N.; Park, J.; Uchida, M.; Shang, S. L.; Zhou, B. C.; et al. Adsorption-Controlled Growth of La-Doped BaSnO$_3$ by Molecular-Beam Epitaxy. *APL Mater.* **2017**, *5*, No. 116107.

(14) Raghavan, S.; Schumann, T.; Kim, H.; Zhang, J. Y.; Cain, T. A.; Stemmer, S. High-Mobility BaSnO$_3$ Grown by Oxide Molecular Beam Epitaxy. *APL Mater.* **2016**, *4*, No. 016106.

(15) Kim, H. J.; Kim, T. H.; Lee, W.; Chai, Y.; Wook, J.; Jae, Y.; Chung, S.; Joong, S.; Sohn, E.; Min, S.; Choi, K.; Hoon, K. Determination of Temperature-Dependent Thermal Conductivity of a BaSnO$_3$ Single Crystal by Using the 3ω Method. *Thermochim. Acta* **2014**, *585*, 16–20.

(16) Maekawa, T.; Kurosaki, K.; Yamanaka, S. Thermal and Mechanical Properties of Polycrystalline BaSnO$_3$. *J. Alloys Compd.* **2006**, *416*, 214–217.

(17) Yasukawa, M.; Kono, T.; Ueda, K.; Yanagi, H.; Wng Kim, S.; Hosono, H. Thermoelectric Properties and Figure of Merit of Perovskite-Type Ba$_{1-x}$La$_x$SnO$_3$ with x = 0.002−0.008. *Solid State Commun.* **2013**, *172*, 49–53.

(18) Prakash, A.; Xu, P.; Wu, X.; Haugstad, G.; Wang, X.; Jalan, B. Adsorption-Controlled Growth and the Influence of Stoichiometry on Electronic Transport in Hybrid Molecular Beam Epitaxy-Grown BaSnO$_3$ Films. *J. Mater. Chem. C* **2017**, *5*, 5730−5736.

(19) Slassi, A. Ab Initio Study of a Cubic Perovskite: Structural, Electronic, Optical and Electrical Properties of Native, Lanthanum- and Antimony-Doped Barium Tin Oxide. *Mater. Sci. Semicond. Process.* **2015**, *32*, 100−106.

(20) Kim, H. M.; Kim, U.; Park, C.; Kwon, H.; Char, K.; Kim, H. M.; Kim, U.; Park, C.; Kwon, H. Thermally Stable Pn-Junctions Based on a Single Transparent Perovskite Semiconductor BaSnO$_3$ Thermally Stable Pn-Junctions Based on a Single Transparent Perovskite Semiconductor BaSnO$_3$. *APL Mater.* **2016**, *4*, No. 056105.

(21) Ganguly, K.; Prakash, A.; Jalan, B.; Leighton, C. Mobility-Electron Density Relation Probed via Controlled Oxygen Vacancy Doping in Epitaxial BaSnO 3. *APL Mater.* **2017**, *5*, No. 056102.

(22) Lindsay, L.; Broido, D. A.; Reinecke, T. L. Thermal Conductivity and Large Isotope Effect in GaN from First Principles. *Phys. Rev. Lett.* **2012**, *109*, No. 095901.

(23) Kundu, A.; Mingo, N.; Broido, D. A.; Stewart, D. A. Role of Light and Heavy Embedded Nanoparticles on the Thermal Conductivity of SiGe Alloys. *Phys. Rev. B* **2011**, *84*, No. 125426.

(24) Peng, B.; Ning, Z.; Zhang, H.; Shao, H.; Xu, Y.; Ni, G.; Zhu, H. Beyond Perturbation: Role of Vacancy-Induced Localized Phonon States in Thermal Transport of Monolayer MoS2. *J. Phys. Chem. C* **2016**, *120*, 29324−29331.

(25) Tachibana, M.; Kolodiazhnyi, T.; Takayama-Muromachi, E. Thermal Conductivity of Perovskite Ferroelectrics. *Appl. Phys. Lett.* **2008**, *93*, No. 092902.

(26) Yamanaka, S.; Hamaguchi, T.; Oyama, T.; Matsuda, T.; Kobayashi, S.; Kurosaki, K. Heat Capacities and Thermal Con-

ductivities of Perovskite Type BaZrO$_3$ and BaCeO$_3$. *J. Alloys Compd.* **2003**, *359*, 1−4.

(27) Tachibana, M. Thermal Conductivity of K$_{1-x}$Li$_x$TaO$_3$ and KTa$_{1-x}$Nb$_x$O$_3$. *Solid State Commun.* **2015**, *221*, 33−35.

(28) Muta, H.; Kurosaki, K.; Yamanaka, S. Thermoelectric Properties of Reduced and La-Doped Single-Crystalline SrTiO3. *J. Alloys Compd.* **2005**, *392*, 306−309.

(29) Giannozzi, P.; Baroni, S.; Bonini, N.; Calandra, M.; Car, R.; Cavazzoni, C.; Ceresoli, D.; Chiarotti, G. L.; Cococcioni, M.; Dabo, I.; et al. QUANTUM ESPRESSO: A Modular and Open-Source Software Project for Quantum Simulations of Materials. *J. Phys. Condens. Matter* **2009**, *21*, No. 395502.

(30) Troullier, N.; Martins, J. L. Efficient Pseudopotentials for Plane-Wave Calculations. II. Operators for Fast Iterative Diagonalization. *Phys. Rev. B* **1991**, *43*, 8861−8869.

(31) Perdew, J. P.; Burke, K.; Ernzerhof, M. Generalized Gradient Approximation Made Simple. *Phys. Rev. Lett.* **1996**, *77*, No. 3865.

(32) Licheron, M.; Jouan, G.; Husson, E. Characterization of BaSnO$_3$ Powder Obtained by a Modified Sol-Gel Route. *J. Eur. Ceram. Soc.* **1997**, *17*, 1453−1457.

(33) Baroni, S.; De Gironcoli, S.; Dal Corso, A.; Giannozzi, P. Phonons and Related Crystal Properties from Density-Functional Perturbation Theory. *Rev. Mod. Phys.* **2001**, *73*, 515−562.

(34) Li, W.; Lindsay, L.; Broido, D. A.; Stewart, D. A.; Mingo, N. Thermal Conductivity of Bulk and Nanowire Mg$_2$Si$_x$Sn$_{1-x}$ Alloys from First Principles. *Phys. Rev. B* **2012**, *86*, No. 174307.

(35) Li, W.; Carrete, J.; Katcho, N. A.; Mingo, N. ShengBTE: A Solver of the Boltzmann Transport Equation for Phonons. *Comput. Phys. Commun.* **2014**, *185*, 1747−1758.

(36) Katcho, N. A.; Carrete, J.; Li, W.; Mingo, N. Effect of Nitrogen and Vacancy Defects on the Thermal Conductivity of Diamond: An *Ab Initio* Green's Function Approach. *Phys. Rev. B* **2014**, *90*, No. 94117.

(37) Katre, A.; Carrete, J.; Dongre, B.; Madsen, G. K. H.; Mingo, N. Exceptionally Strong Phonon Scattering by B Substitution in Cubic SiC. *Phys. Rev. Lett.* **2017**, *119*, No. 075902.

(38) Karamargin, M. C.; Reynolds, C. A.; Lipschultz, F. P.; Klemens, P. G. Lattice Thermal Conductivity and Deviations from Matthiessen's Rule for Dilute Alloys of Tin with Cadmium. *Phys. Rev. B* **1972**, *6*, 3624−3633.

(39) Wu, X.; Yang, N.; Luo, T. Unusual Isotope Effect on Thermal Transport of Single Layer Molybdenum Disulphide. *Appl. Phys. Lett.* **2015**, *107*, No. 191907.

(40) Feng, T.; Qiu, B.; Ruan, X. Coupling between Phonon-Phonon and Phonon-Impurity Scattering: A Critical Revisit of the Spectral Matthiessen's Rule. *Phys. Rev. B* **2015**, *92*, 1−5.

(41) Lambin, P.; Vigneron, J. P. Computation of Crystal Green's Functions in the Complex-Energy Plane with the Use of the Analytical Tetrahedron Method. *Phys. Rev. B* **1984**, *29*, 3430−3437.

(42) Esfarjani, K.; Chen, G.; Stokes, H. T. Heat Transport in Silicon from First-Principles Calculations. *Phys. Rev. B* **2011**, *84*, No. 085204.

(43) Kim, B. G.; Jo, J. Y.; Cheong, S. W. Hybrid Functional Calculation of Electronic and Phonon Structure of BaSnO$_3$. *J. Solid State Chem.* **2013**, *197*, 134−138.

(44) Ward, A.; Broido, D. A.; Stewart, D. A.; Deinzer, G. Ab Initio Theory of the Lattice Thermal Conductivity in Diamond. *Phys. Rev. B* **2009**, *80*, No. 125203.

(45) Wu, X.; Lee, J.; Varshney, V.; Wohlwend, J. L.; Roy, A. K.; Luo, T. Thermal Conductivity of Wurtzite Zinc-Oxide from First-Principles Lattice Dynamics − a Comparative Study with Gallium Nitride. *Sci. Rep.* **2016**, *6*, No. 22504.

(46) Ratsifaritana, C. A.; Klemens, P. G. Scattering of Phonons by Vacancies. *Int. J. Thermophys.* **1987**, *8*, 737−750.

(47) Park, C.; Kim, U.; Ju, C. J.; Park, J. S.; Kim, Y. M. High Mobility Field Effect Transistor Based on BaSnO$_3$ with Al$_2$O$_3$ Gate Oxide. *Appl. Phys. Lett.* **2014**, *105*, No. 203503.

(48) Okuda, T.; Nakanishi, K.; Miyasaka, S.; Tokura, Y. Large Thermoelectric Response of Metallic perovskites:Sr$_{1-x}$La$_x$TiO$_3$. *Phys. Rev. B* **2001**, *63*, No. 113104.

(49) Yu, C.; Scullin, M. L.; Huijben, M.; Ramesh, R.; Majumdar, A. Thermal Conductivity Reduction in Oxygen-Deficient Strontium Titanates. *Appl. Phys. Lett.* **2008**, *92*, No. 191911.

(50) Wang, Y.; Sui, Y.; Wang, X.; Su, W.; Liu, X.; Fan, H. J. Thermal Conductivity of Electron-Doped CaMnO3 Perovskites: Local Lattice Distortions and Optical Phonon Thermal Excitation. *Acta Mater.* **2010**, *58*, 6306−6316.